PERGAMON

International Journal of Heat and Mass Transfer 42 (1999) 323–343

International Journal of HEAT and MASS TRANSFER

Heat transfer simulation in vertical cylindrical enclosures for supercritical Rayleigh number and arbitrary side-wall conductivity

A. Ivančić*, A. Oliva, C. D. Pérez Segarra, M. Costa

Laboratori de Termotècnia i Energètica, Departamento Màquines i Motors Tèrmics. Universitat Politècnica de Catalunya, Colom 9, 08222 Terrassa, Barcelona, Spain

Received 28 March 1997; in final form 26 February 1998

Abstract

In the present paper the heat transfer in a vertical cylinder heated from below has been analysed; the influence of the Rayleigh number, Prandtl number, aspect ratio and lateral wall thermal boundary condition has been examined in the range of $1 \leqslant A \leqslant 5$ and $1{\cdot}10^{-2} \leqslant Pr \leqslant 1{\cdot}10^{5}$. The time-dependent flow onsets and their fundamental frequencies are indicated for several low Prandtl numbers ($Pr \leqslant 5{\cdot}10^{-2}$). For $Pr > 1{\cdot}10^{-1}$, no evidence of oscillatory flow has been found in the studied range of parameters. In order to simulate the lateral walls with thermal boundary conditions different than the two idealised cases (adiabatic wall and perfectly conducting wall), the heat transfer through the solid wall is included by the simultaneous calculation of both fluid and solid domain (conjugated heat transfer).

Nomenclature

$A = H/2R$ aspect ratio
a discretization coefficients
$C = k_f R/k_s e$ wall admittance
c_p specific heat at constant pressure
e wall thickness
F mass flow rate
f frequency
$f^* = fH^2/\alpha$ dimensionless frequency
g gravitational acceleration
H cylinder height
k thermal conductivity
$Nu = \int_s (V_z T - (\partial T/\partial z))\,\mathrm{d}s$ surface average Nusselt number
p pressure
$Pr = \mu c_p/k$ Prandtl number
R cylinder radius
r radial coordinate
$Ra = g\beta\rho H^3(T_h - T_c)/\mu\alpha$ Rayleigh number
$Re = \rho V_0 R/\mu$ Reynolds number
S source term
T temperature
t time
v velocity
z axial coordinate.

Greek
$\alpha = k/\rho c_p$ thermal diffusivity
β thermal expansion coefficient
Γ diffusion coefficient
Δ distance
μ dynamic viscosity
ρ density
θ azimuthal coordinate
ϕ dependent variable.

Subscripts
c cold
cr critical value
f fluid
h hot
i interface (liquid/solid)
r radial component
s solid

* Corresponding author.

0017–9310/98 $19.00
PII: S0017–9310(98)00113–6

z axial component
θ azimuthal component
0 reference value.

Operators

$$\nabla = \frac{1}{r}\frac{\partial}{\partial r}r + \frac{1}{r}\frac{\partial}{\partial \theta} + \frac{\partial}{\partial z}$$

$$\frac{D}{Dt} = \frac{\partial}{\partial t} + v_r\frac{\partial}{\partial r} + \frac{v_\theta}{r}\frac{\partial}{\partial \theta} + v_z\frac{\partial}{\partial \theta}$$

1. Introduction

The phenomenon of laminar convection in fluids framed in a cylindrical enclosure, driven by density difference and/or by external force, often occurs in technical applications and industrial processes. The fluid motion caused by the phenomenon has a great impact on the working characteristic of devices and processes where it occurs. The problem arises in applications such as: tanks for energy or material storage, electric motor shells, transparent insulation cells, etc. Buoyancy convection plays an important role in the process of solidification or crystal growth of semiconductors, which are the materials of great importance in modern electronics. Natural convection phenomenon has a decisive influence on creation of crystal defects and inhomogenities. As such irregularities reduce material quality, the goal of the technological process is to control the convective transport.

The buoyancy driven flow in fluid layer heated from below, also known as Rayleigh–Bénard convection, is one of the fluid dynamic topics widely analysed. One of the fundamental aspects is the determination of the convective threshold (Ra_{cr}) and the influence of initial and boundary conditions on it. Several contributions concern the Rayleigh–Bénard problem in cylindrical enclosure. The linear stability analysis has been applied by Gershuni and Zhukhovitskii [1] and Charlson and Sani [2] in order to find the critical Rayleigh number (Ra_{cr}) and to describe the flow structure, for the several system parameters. These analyses have been made for perfectly insulated and perfectly conducting lateral wall (idealised thermal boundary conditions). Buell and Catton [3] used linear stability analysis to find the convective threshold considering an arbitrary thermal conductivity in the lateral wall.

Experimental observations and measurements of buoyancy driven motion have been performed by Figliola [4] for $A = 1$, Azouni and Grenet [5], Olsaen and Rosenberger [6], Müller et al. [7, 8] and recently by Kamotani et al. [9], for tall cylinders ($A > 1$). Müller et al. [7] carried out the experiments with the cylinders made of three different materials: glass, PMMA and aluminium, all of them of $A = 5$ and filled with water ($Pr \approx 7$). The evolution of the spatial structures of the convective motion with increase of Ra has been described. The influence of the wall material on Ra_{cr} has also been discussed. Müller et al. [8] analysed convection in the cylinders with aspect ratio in range of $0.5 \leqslant A \leqslant 5$ filled with water ($Pr = 6.7$) and melted galium ($Pr \approx 2.10^{-2}$). They gave the stability diagrams with the convective threshold and the unsteady flow threshold distinguishing the steady, periodic and turbulent ranges. For water the unsteady flow appears for $Ra > 30\ Ra_{cr}$.

The numerical methods have also been applied in order to investigate the phenomenon. Numerical simulation has been carried out by Crespo et al. [10–12]; analysis of the effects of aspect ratio change on spatial flow configuration and stability of flow solution to initial conditions has been performed in [10]; effects of Prandtl number on flow patterns have been studied in [11] as well as the convective threshold and critical aspect ratio between axisymmetric and asymmetric flow mode [12]; in those works, the results are widely compared with data obtained by linear stability analysis [1–3]. Flow transition from 2D axisymmetric to 3D asymmetric spatial structure in flat cylinder ($A = 0.5$) and oscillatory convection regimes have been simulated by Neumann [13]. A transition route from steady laminar to turbulent regime for cylinder of $A = 1.5$ has been recently presented by Ivančić et al. [27]. Inclination effects on heat transfer in cylindrical cavity are examined by Schneider and Straub [14]; these numerical results are also supported by experimental verification. In this study a correlation of the Nusselt number as function of Rayleigh number, aspect ratio and inclination angle has been established.

The work of Buell and Catton [3] takes into account the side-wall thermal boundary condition within the wide spectra of the two idealised extremes (adiabatic and perfectly conducting boundary condition); no other papers, to the best of the author's knowledge, concerning the cylindrical enclosures analyse systematically this parameter. The transition from steady to time-dependent flow in cylindrical enclosures is the other topic which deserves more attention than it has been given up to now.

The principal purpose of this study is to analyse the influence of the aspect ratio, the Rayleigh number, the Prandtl number and the lateral thermal boundary condition on convective heat transfer in vertical cylinders. For that purpose we developed a three-dimensional, transient simulation code which predicts heat transfer and flow patterns in cylindrical enclosures with different side-wall thermal boundary conditions. In Section 2, the physical problem is established and its mathematical formulation is presented; in Section 3 some numerical aspects are explained and the numerical code is validated. Three aspects of natural convection in a vertical cylinder are analysed in Section 4: the first one is the influence of aspect ratio on the convective threshold and heat transfer in the range of $1 \leqslant A \leqslant 5$, the second one is the influence of the Prandtl number in range of $1 \cdot 10^{-2} \leqslant Pr \leqslant 1 \cdot 10^{5}$

and the last one is the influence of the lateral thermal boundary condition on heat transfer. The lateral thermal boundary condition is analysed using solid thermal conductivity values from zero to infinite, that is from adiabatic to perfectly conducting side-wall. The side-wall influence is parametrized by a wall admittance. The comparison with experimental and theoretical data is carried out. The oscillatory flow limits and corresponding fundamental frequencies are found for the low Prandtl number fluids ($1\cdot10^{-2} \leqslant Pr \leqslant 5\cdot10^{-2}$). In Section 5 the main conclusions are drawn.

2. Physical model and mathematical description

2.1. Governing equations

The phenomenon of laminar flow of Newtonian fluids in a vertical cylindrical domain, after introducing the Boussinesq approximation, is governed by the mass, momentum and energy equations:

$$\nabla\cdot\vec{v} = \vec{0} \tag{1}$$

$$\rho\frac{\mathrm{D}\vec{v}}{\mathrm{D}t} = -\nabla p + \mu\nabla^2\vec{v} + \rho_0\vec{g}[1-\beta(T-T_0)] \tag{2}$$

$$\rho C_\mathrm{p}\frac{\mathrm{D}T}{\mathrm{D}t} = k\nabla^2 T \tag{3}$$

The Boussinesq approximation assumes that the density is constant in all terms except in the buoyancy term in the momentum equation; the other physical properties of fluid are taken as constants.

In the cylindrical coordinate system, the above governing equations can be casted in the generic form of the convection–diffusion equation:

$$\frac{\partial(\rho\phi)}{\partial t} + \frac{1}{r}\left(\frac{\partial(\rho r v_r\phi)}{\partial r} + \frac{\partial(\rho v_\theta\phi)}{\partial\theta} + \frac{\partial(\rho r v_z\phi)}{\partial z}\right) = \frac{\Gamma}{r}\left[\frac{\partial}{\partial r}\left(r\frac{\partial\phi}{\partial r}\right) + \frac{\partial}{\partial\theta}\left(\frac{1}{r}\frac{\partial\phi}{\partial\theta}\right) + \frac{\partial}{\partial z}\left(r\frac{\partial\phi}{\partial z}\right)\right] + S \tag{4}$$

where ϕ, Γ and S are the dependent variable, the diffusion coefficient and the source term respectively. The meaning for every particular governing equation is written in Table 1.

2.2. Geometry and boundary conditions

The attention is focused on buoyancy driven, natural convection in vertical cylindrical vessel of radius R, wall thickness e and height H, heated from below. The geometry of the problem is shown in Fig. 1. The phenomenon arises as a consequence of differently heated top and bottom cylinder bases. The flow field and the heat transfer are determined by the following dimensionless parameters: aspect ratio A, Prandtl number Pr, wall admittance C and Rayleigh number Ra (for definition see Nomenclature).

The set of governing equations (1)–(3) is completed by the following boundary conditions:

for the momentum equations, at the solid–liquid interface, no slip boundary condition is applied

$$\begin{aligned} v_r, v_\theta, v_z = 0 \quad &\text{at } r = R;\ 0 \leqslant \theta \leqslant 2\pi \quad \text{and} \quad 0 \leqslant z \leqslant H \\ &\text{at } z = 0;\ 0 \leqslant r \leqslant R \quad \text{and} \quad 0 \leqslant \theta \leqslant 2\pi \\ &\text{at } z = H;\ 0 \leqslant r \leqslant R \quad \text{and} \quad 0 \leqslant \theta \leqslant 2\pi \end{aligned} \tag{5}$$

while the thermal boundary conditions are isothermal horizontal cylinder bases

$$\begin{aligned} T(r,\theta,z=0) &= T_\mathrm{h} \\ T(r,\theta,z=H) &= T_\mathrm{c} \end{aligned} \tag{6}$$

and external adiabatic lateral wall

$$\left.\frac{\partial T}{\partial r}\right|_{r=R+e} = 0 \tag{7}$$

The parametrization of the lateral solid wall is accomplished by means of the wall admittance C, a dimensionless number defined as:

$$C = \frac{k_\mathrm{f}R}{k_\mathrm{s}e} \tag{8}$$

where k_f and k_s are the thermal conductivities of fluid and wall respectively and e is the wall thickness. The idealised extreme cases: $C = 0$ for a perfectly conducting wall and $C = \infty$ for a perfectly insulating wall can be modeled using appropriate boundary condition on fluid domain without taking into account the solid wall, while for the amid cases ($0 < C < \infty$) the model for conjugated heat transfer is needed.

Even prescribing both the geometry and the boundary conditions as axisymmetric ones the flow may not be axisymmetric. The calculations of Buell and Catton [3] based on the linear stability theory predict a change between symmetric and asymmetric flow field on aspect ratio of $A_\mathrm{c} = 0.56$ for the adiabatic sidewall, and for $A_\mathrm{c} = 0.65$ for the perfectly conducting sidewall. The axisymmetric flow fields appear for the values lower than the A_c, while the asymmetric ones appear for $A > A_\mathrm{c}$. In case of $A \geqslant A_\mathrm{c}$ the three-dimensional model is necessary to simulate the flow. The numerical calculations of Crespo et al. [12] situate the flow mode interchange near $A_\mathrm{c} = 0.625$ for the perfectly conducting sidewall. However, the flow field for the aspect ratio range chosen in this study ($1 \leqslant A \leqslant 5$) is strongly asymmetric and thus three-dimensional.

3. Numerical aspects

3.1. Discretization

A grid is generated in the polar–cylindrical coordinate system to cover the domain of interest; a typical control

Table 1
Dependent variables, diffusion coefficients and source terms

Equation	Φ	Γ	S
Mass	1	0	0
r momentum	V_r	μ	$\rho\frac{v_\theta^2}{r}-\frac{\partial P}{\partial r}-\mu\frac{2}{r^2}\frac{\partial v_\theta}{\partial\theta}-\mu\frac{v_r}{r^2}$
θ momentum	V_θ	μ	$-\rho\frac{v_\theta v_r}{r}-\frac{1}{r}\frac{\partial P}{\partial\theta}+\mu\frac{2}{r^2}\frac{\partial v_r}{\partial\theta}-\mu\frac{v_\theta}{r^2}$
z momentum	V_z	μ	$-\frac{\partial P}{\partial z}+\rho g\beta(T-T_0)$
Energy	T	λ/c_p	0

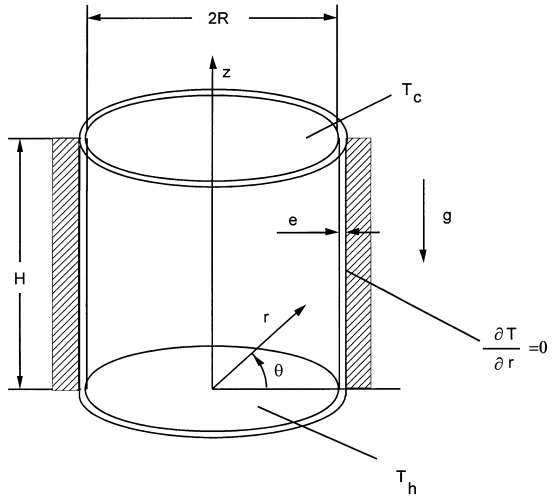

Fig. 1. Scheme of the analysed geometry along with the thermal boundary conditions.

volume (CV) is shown in Fig. 2a. The common convection–diffusion equation is integrated over this CV and each term in the resulting integral balance is approximated in terms of the discrete values of ϕ in the nodal points. In order to avoid the well known checkerboard problem, the momentum equations are discretized over a staggered grid arrangement (Fig. 3). The algebraic equations obtained after discretization get the standard linearized form (see e.g., [19]:

$$a_p\phi_p=\sum_{nb=\mathrm{I,O,C,A,T,B}}a_{nb}\phi_{nb}+S \tag{9}$$

where a are the discretization coefficients (subindexes meaning location: I—inner, O—outer, C—clockwise, A—anticlockwise, T—top, B—bottom), S is a source term and ϕ represents discrete values of the dependent variable concerning the corresponding CV.

The particularity of polar–cylindrical coordinate system is that its origin in general does not coincide with a physical boundary. The differential equation describing transport phenomena (equation 4) includes terms like $(1/r)$ and $(\partial/\partial r)$ that become singular at the origin of the radial coordinate; this leads to some computational difficulties. The problem is avoided if boundary conditions can be prescribed at the axis; either specified variables or its derivatives (in case of any kind of symmetry—axial, plane or antisymmetry) is sufficient to prevent the mentioned difficulty. Vahl Davis [15] comments on the problem for arbitrary boundary conditions, suggesting generating the mesh without nodes at the axis, i.e., the computational domain is extended up to a thin cylinder around the z axis, and to approximate radial derivatives for the first inner point by a second order forward differencing formula. After Vahl Davis, the omitting of a sufficiently small part of the domain does not influence on the calculation accuracy. This method has been widely used (Crespo et al. [10–12], Leong and Vahl Davis [16], Bontoux et al. [17]). In literature other proposals exist about the singularity treatment as one by Schneider and Straub [14] who introduced a cylinder-shape CV near the axis. Alternative choice may be the use of nonstructured grids or so-called Chimera grids.

In the present study a different approach has been adopted. Firstly, the grid is generated up to the axis. The differential equations for the v_θ, v_z and the scalar quantities are discretized in the same manner for all the CV of the computational domain; the CVs at the axis are treated in the same way taking into account that inner face area is equal to zero. The radial velocity component (v_r) is calculated in staggered CVs in the radial direction. As a consequence the center remains uncovered for v_r equation. To prevent that, an additional CV in the radial momentum equation is included to ensure information about v_r for the first 'regular' CV. In this way the whole calculation domain remains covered. The additional CV is located in just one pressure CV, that means that there

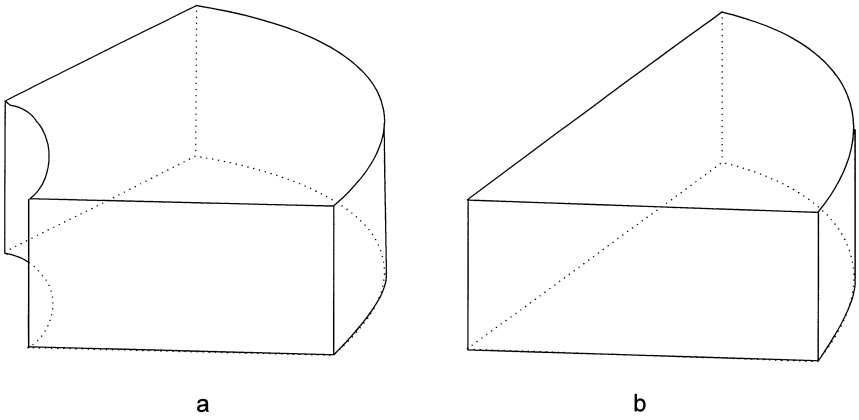

Fig. 2. (a) Typical control volume un the cylindrical system; (b) first control volume in the cylindrical coordinate system.

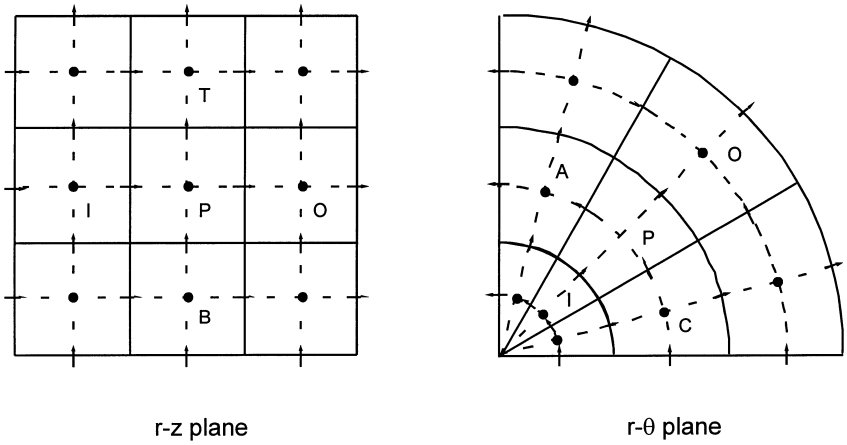

Fig. 3. Grid arrangement in the cylindrical coordinate system.

is no pressure gradient in it ($\partial p/\partial r = 0$). The basic advantage of the present treatment is its simplicity which involves very few additional steps in the numerical code without significant penalising of the CPU time.

Some addends of the source terms obtained after discretization of momentum equations are nonlinear (see Table 1); these terms require linearization to ensure numerical stability. The linearization has been done in the standard form:

$$S = S_c + S_P \phi_P \tag{10}$$

In order to enhance convergence and avoid numerical instability, the S_c and S_p terms are evaluated in this way:

$$S_c = \max(NLT, 0)\phi_P^0 \quad S_p = \min(NLT, 0) \tag{11}$$

where NLT are the ϕ-dependent source term addends and ϕ_p^0 is the nodal value of ϕ at the previous iteration.

The calculation procedure follows the SIMPLEC [18] algorithm along with a fully implicit method; time derivatives are approximated using a first order backward Euler scheme. The system of linear algebraic equations is solved using the TDMA [19] and occasionally the MSIP [20]; both solvers are arranged for cyclic conditions in θ direction. As a convergence criteria the mass source term (S in the continuity equation) has been used, requiring to be less than 10^{-8} in every CV. The diffusion term is calculated by the central difference scheme. Different discretization schemes have been used to approximate the convective terms: first order upwind (FOU), PLDS [19], second order central difference (CDS), QUICK [21], SMART [22], MUSCL [31], SOUCUP [32]. When a higher order (h.o.) accuracy numerical schemes (CDS, QUICK, SMART, MUSCL, SOUCUP) are used for the convective term, upwind differencing is applied as a first step and the additional value is summed up to the source term and calculated in a deferred way as proposed by Khosla and Rubin [29]:

$$F\phi = F\phi^{FOU} + \underbrace{F(\phi^{h.o.} - \phi^{o,FOU})}_{\text{source}} \tag{12}$$

The advantage of this kind of numerical treatment is two-fold: firstly, the numerical stability of the code is improved, and secondly, when the 13-point computational molecule is applied, the matrix structure is the same as for a 7-point computational molecule that allows the use of the same solver for linear equation system for all the discretization schemes applied. In this way, the usual structure of pressure-correction type codes is preserved without necessity of rewriting any part of the code except the new source addend.

When the heat transfer in the solid lateral wall is taken into account, the calculation for fluid and solid parts is made simultaneously for the whole domain. As for the solid region, only the energy equation is needed: the matrix corresponding to that equation is simply extended to cover the solid part of calculation domain. The thermal conductivity on the interface solid/fluid is deduced equating the thermal conductances for a multi-layer cylinder (k_f, k_s) with the thermal conductance for a single-layer cylinder ($\bar{k}$):

$$\bar{k} = \frac{\ln\frac{r_s}{r_f}}{\frac{1}{k_f}\ln\frac{r_i}{r_f} + \frac{1}{k_s}\ln\frac{r_s}{r_i}} \tag{13}$$

where $\bar{k}$ is the average thermal conductivity, k_f and k_s are thermal conductivities of the fluid and solid wall respectively, and r_i, r_f and r_s are the radii shown in Fig. 4.

3.2. Validation of the space discretization

In order to check the behavior of the arrangement introduced in the vicinity of the axis, two tests have been performed. With these tests the intention is to check only the approach introduced for treatment of the CVs near the axis in the polar-cylindrical coordinate system, hence the test has been carried out in 2D, in r–θ plane. We consider these tests specially suitable for the validation because the exact solution of the problems is known. Besides these tests, other cases are used for validation of the code, but due to space limitation we expose just what we consider most interesting for the particular treatment introduced for the polar-cylindrical coordinates.

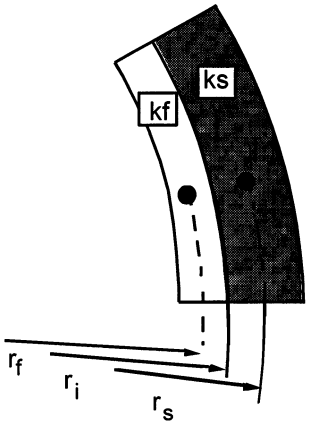

Fig. 4. Solid–liquid boundary.

As a first test, the benchmark case proposed by Smith and Hutton [30] has been performed (Fig. 5). This problem is widely used for the numerical schemes and codes testing. The test consists in solving the scalar (e.g. temperature) field in the domain with the known velocity field. For the particular case of diffusion-free flow ($\Gamma = 0$) the analytical solution of the scalar field is known.

In the original form, in [30], the problem is established in the Cartesian coordinates considering a rectangular domain: $-1 \leqslant x \leqslant 1$, $0 \leqslant y \leqslant 1$, where the velocity field is given by:

$$v_x = 2y(1-x^2); v_y = -2x(1-y^2) \tag{14}$$

and the temperature profile on the inlet ($-1 \leqslant x \leqslant 0$, $y = 0$) is given as a step transition form 0 to 2:

$$T_{in} = 1 + \tanh[\sigma(1+2x)] \tag{15}$$

where σ is the transition steepness parameter; in the present study a value of $\sigma = 100$ is used representing a very sharp transition. For diffusion-free case ($\Gamma = \infty$) the temperature field is solved analytically giving:

$$T(x,y) = 1 + \tanh[\sigma(1-2\sqrt{1-(1-x^2)(1-y^2)}) \tag{16}$$

For the testing in the polar–cylindrical coordinates, the middle part of the rectangular domain is selected, as shown in Fig. 5. After coordinates transformation, the velocity field and the temperature boundary condition are specified for the cylindrical domain.

The calculated temperature profiles are compared with the analytical solution in the section $x = 0$ marked as A–A in Fig. 5. The test has been carried out with five different numerical schemes: FOU, QUICK, SMART, SOUCUP and MUSCL, and on five grids: 10×20, 10×40, 15×40, 20×40 and 20×60 in r, θ direction. Figure 6 shows the results obtained by the different numerical schemes on 10×20 grid. The FOU scheme exhibits smoothed temperature profile due to false diffusion, the typical problem of the first-order schemes, while all the other, higher order schemes are noticeably sharper. The QUICK scheme shows very sharp temperature profile but with spatial oscillations. The best results are achieved by the SMART numerical scheme. The grid dependent solutions for the FOU and SMART schemes are shown in Fig. 7. The important conclusion is that the temperature profile remains smooth and undisturbed near the coordinate center. This means that the approach introduced to treat the coordinate center do not affect the solution of the temperature profile.

Test 2 corresponds to a uniform stream flow (Fig. 8). The boundary conditions for this unidimensional parallel flow in the polar–cylindrical coordinate system are given as:

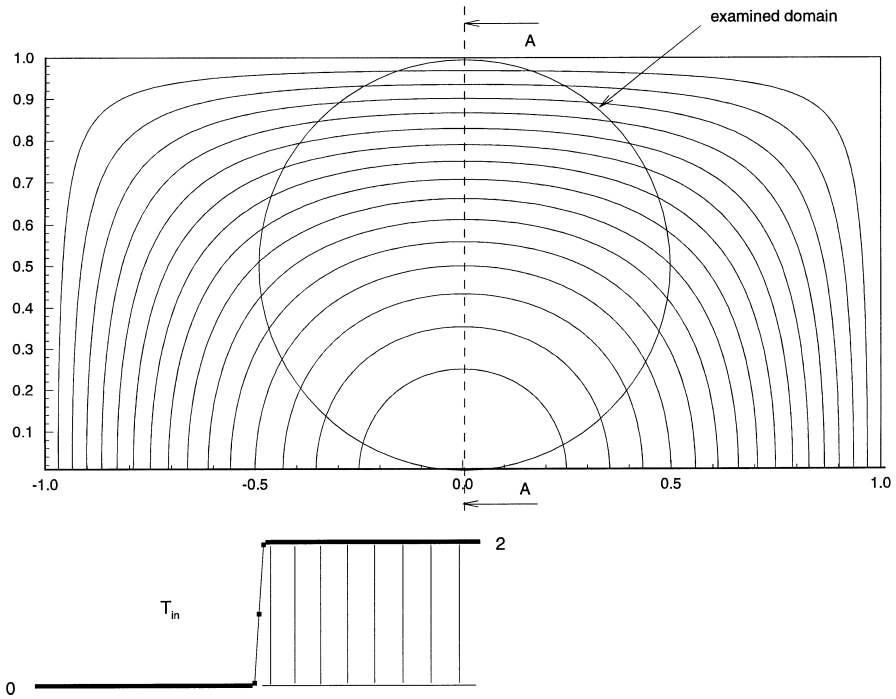

Fig. 5. Test 1 : streamline pattern and inlet temperature profile.

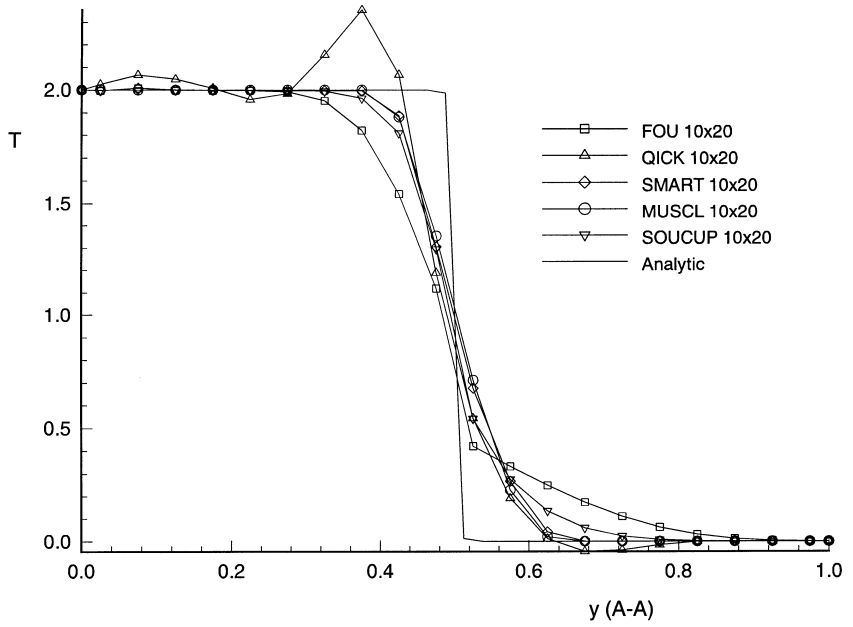

Fig. 6. Test 1 : temperature profiles calculated by different numerical schemes on a grid 10×20.

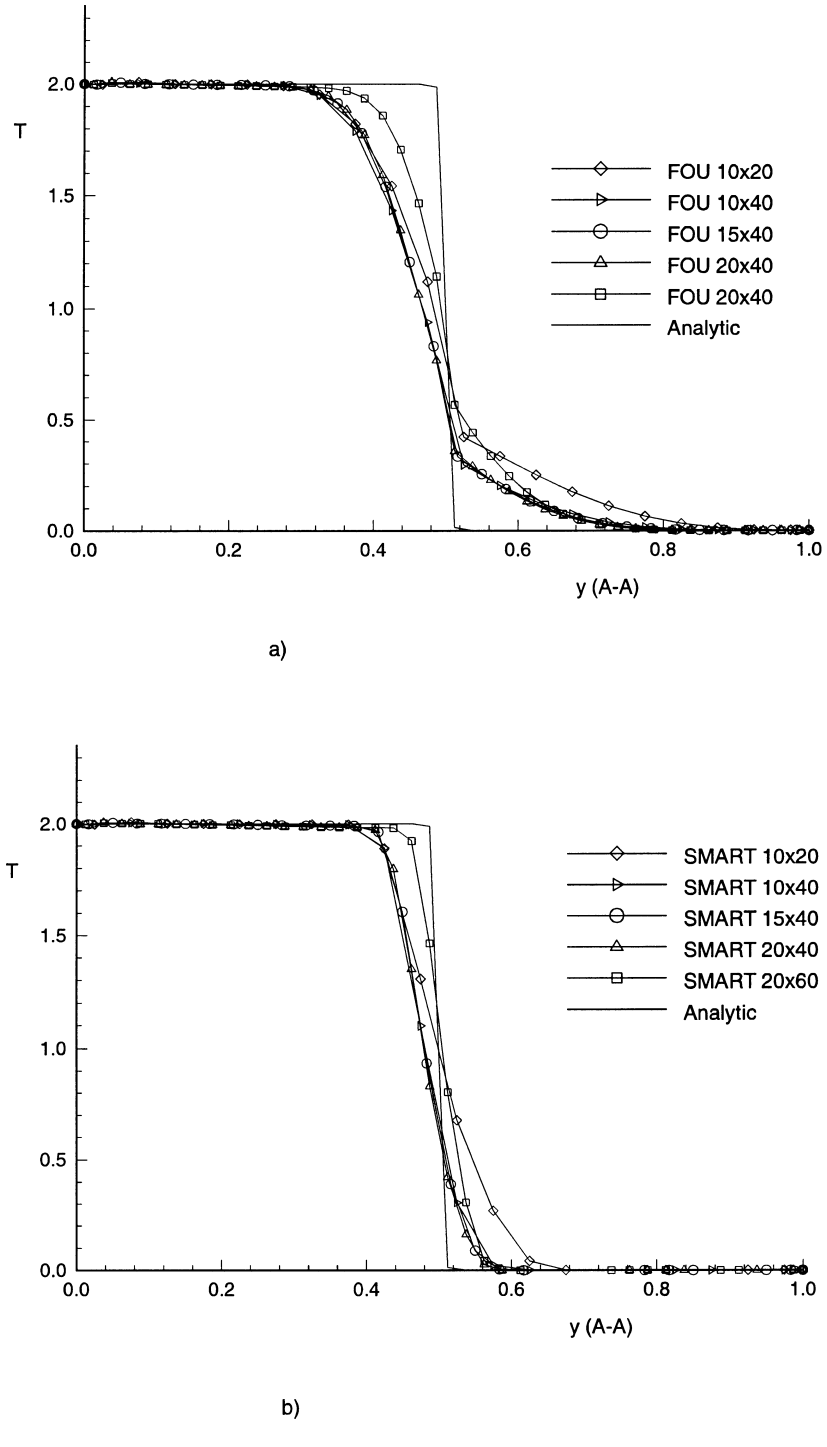

Fig. 7. Test 1 : temperature profiles calculated by different grids using (a) FOU scheme and (b) SMART scheme.

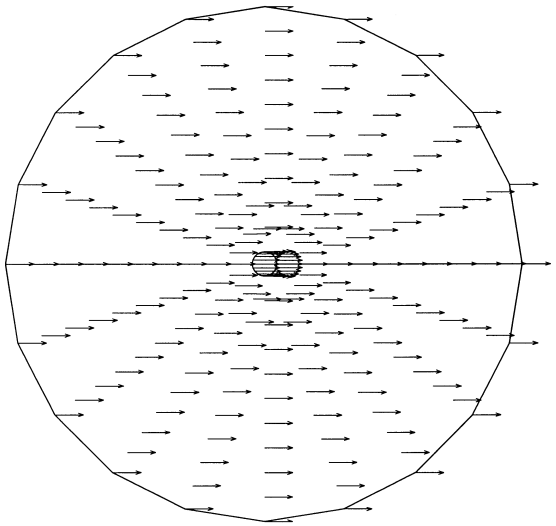

Fig. 8. Test 2: uniform stream flow; velocity field obtained by CDS numerical scheme on 10×20 CV grid.

$$v_r(r = R, \theta) = v\cos\theta\,; v_\theta(r = R, \theta) = -v\sin\theta \qquad (17)$$

The test has been done with four different grids: 10×20, 16×32, 20×40 and 30×60 CVs in r and θ directions. In Fig. 9, the velocity profiles for $V_r(\theta = 0,\ \pi)$ and $V_\theta(\theta = \pi/2,\ 3\pi/2)$ are shown; the absolute values of V_r are presented rather than relative because of the change of sign at the origin. The comparison in that figure is made between the exact solution and the numerical solution on 10×20 CV grid. A certain velocity deviation near the center has been observed. The results obtained by the FOU scheme achieves the biggest deviation—19% with respect to exact solution (exact solution is represented by horizontal solid line). The PLDS gives better results (6% deviation). The second and higher order schemes allow results with deviation up to 1.5% for the 10×20 grid. Figure 10 represents the influence of the grid refinement on the relative error. Refining the discretization grid, the relative error decreases. The error in the direction perpendicular on the flow ($V_\theta(\theta = \pi/2,\ 3\pi/2)$) is more pronounced.

The results of both tests draw well the expected temperature and flow patterns using at least second order numerical schemes; PLDS and FOU are not a good choice for the arrangement applied. The results presented in the following sections have been carried out using the CDS numerical scheme, except the simulation of the oscillatory flows (Section 4.4) which has been performed by the SMART numerical scheme.

4. Numerical results

4.1. Influence of the grid

The influence of grid refinement on heat transfer has been examined. The Nusselt number values have been

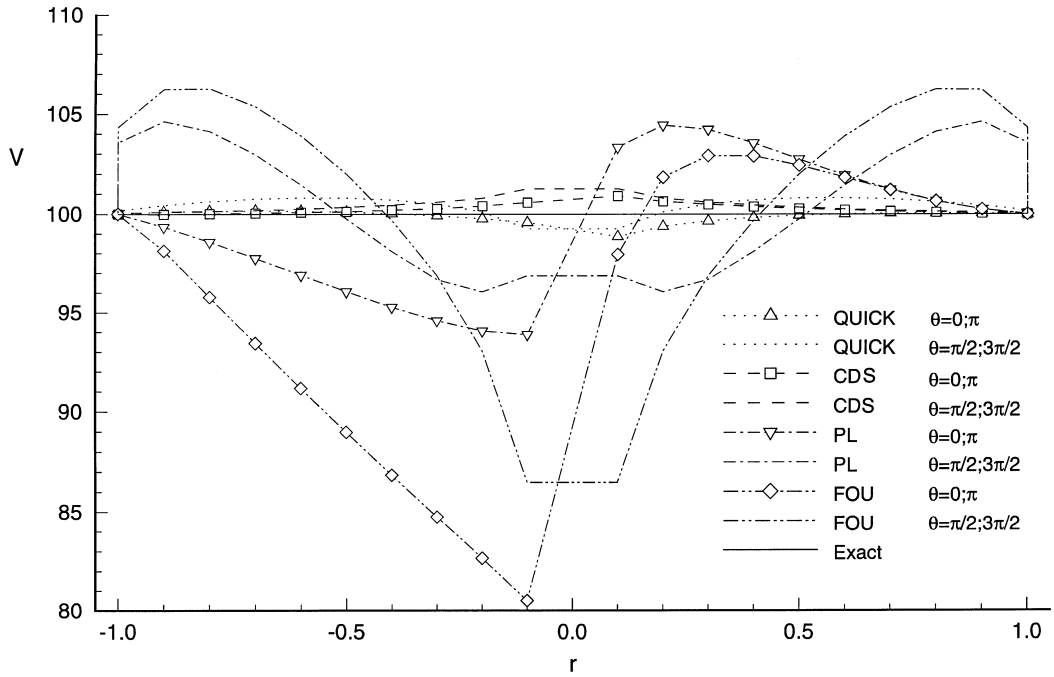

Fig. 9. Test 2: velocity profiles for $V_r(\theta = 0, \pi)$ and $V_\theta(\theta = \pi/2, 3\pi/2)$ obtained by different numerical schemes on a grid of 10×20.

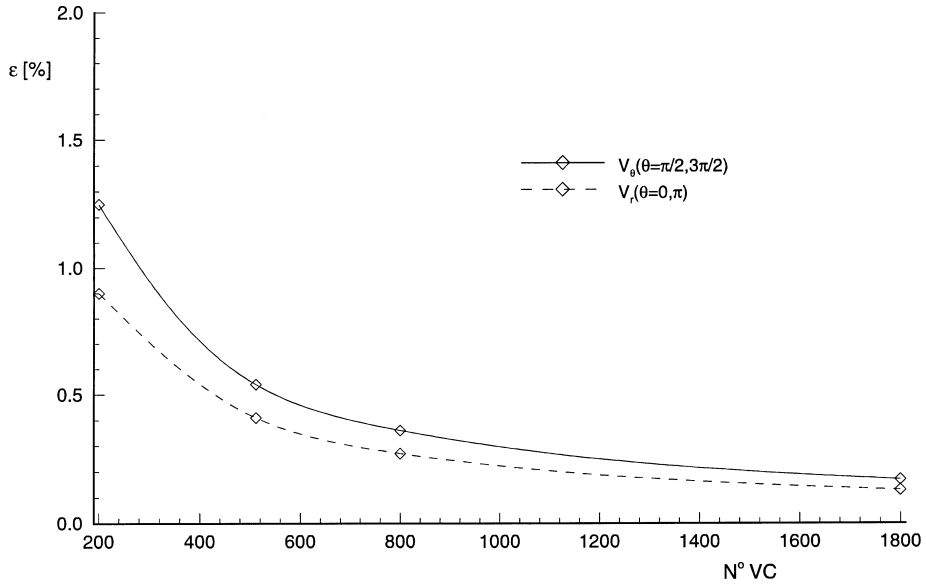

Fig. 10. Test 2: maximum relative error vs number of control volumes.

compared for four different uniform grids ($5\times10\times10$; $10\times20\times20$; $15\times30\times30$; $20\times36\times36$ in r, θ, z direction) in the range of $Ra_{cr} < Ra < 2Ra_{cr}$ for a cylinder of aspect ratio $A = 1$ and $Pr = 1$. No qualitative difference in the spatial flow structure obtained by different grids has been observed, but certain discrepancy in quantitative sense exists. Refining the grid results, in general, in a smaller maximum velocity and somewhat lower Nusselt number. Discrepancy in Nu increases for higher Ra. For the highest Rayleigh number tested, $Ra = 1\cdot10^4$ there is a difference of 9.3% for $Nu_{(5\times10\times10)}$, 2.4% for $Nu_{(10\times20\times20)}$ and 0.5% for $Nu_{(15\times30\times30)}$ with respect to $Nu_{(20\times36\times36)}$ (Fig. 11). In general, the data presented in this paper were calculated with a grid of $10\times20\times20$ control volumes in r, θ, z direction, which does not completely offer grid independent solution but it was considered as a good compromise between accuracy and CPU time. When the solid wall is introduced, a grid of $(10+1)\times20\times20$ has been used.

4.2. Convective threshold

The convective motion starts when the Rayleigh number exceeds a critical value. For $Ra < Ra_{cr}$ no motion occurs. Stratified disposition in fluid body exists and heat transfer is leaded only by diffusion ($Nu = 1$). For a horizontal infinite layer, convective onset takes place for $Ra_{cr} = 1707.7$ [23]. When the fluid is bounded the convective onset is displaced toward a higher Ra value due to the stabilising effect of the sidewall. The critical Rayleigh number depends both on the boundary conditions and the geometry and not on the physical properties of the fluid, hence the critical value Ra_{cr} does not depend on the Prandtl number (except for the limited case $Pr \to 0$, see [25]). In the examined range of the aspect ratio, the first convective motion corresponds to a helical single-roll, which appears as a single vortex in the vertical symmetry plane, and in its orthogonal plane there are four equal vortices, each one occupying one quarter of the section (Fig. 12). Between these two planes there are sections with a main roll and two smaller secondary counter-rolls in the corners. With the increasing of Ra the main vortex inclinates and later, at $Ra \geqslant 5\ Ra_{cr}$ for water, according to experimental data by Müller et al. [8], two secondary vortices also appear in opposite corners of the vertical symmetry plane. Sometimes it is convenient to analyse and to discuss about characteristic sections, i.e. vertical symmetry and orthogonal planes, due to the spatial complexity of the convection motion. These planes appear in arbitrary position in the cylinder, they are not conditioned by the numerical algorithm; furthermore they are introduced in the subsequent analysis of the results of the calculation. However, one should keep in mind the spatial structure of the flow; Figs 13A–C show the characteristic trajectories in order to make clear the three-dimensional fluid movement inside the cylinder. The particles make outward spiral motion near the vertical symmetry plane, then leave that plane and later follow helical paths going back toward the symmetry plane. While helical movement occurs, the radius of circulation decreases (Figs 13A and C). It is interesting to note that the described trajectories are, in a certain way, similar to the ones presented by Kessler [24] for natural convection in rectangular boxes.

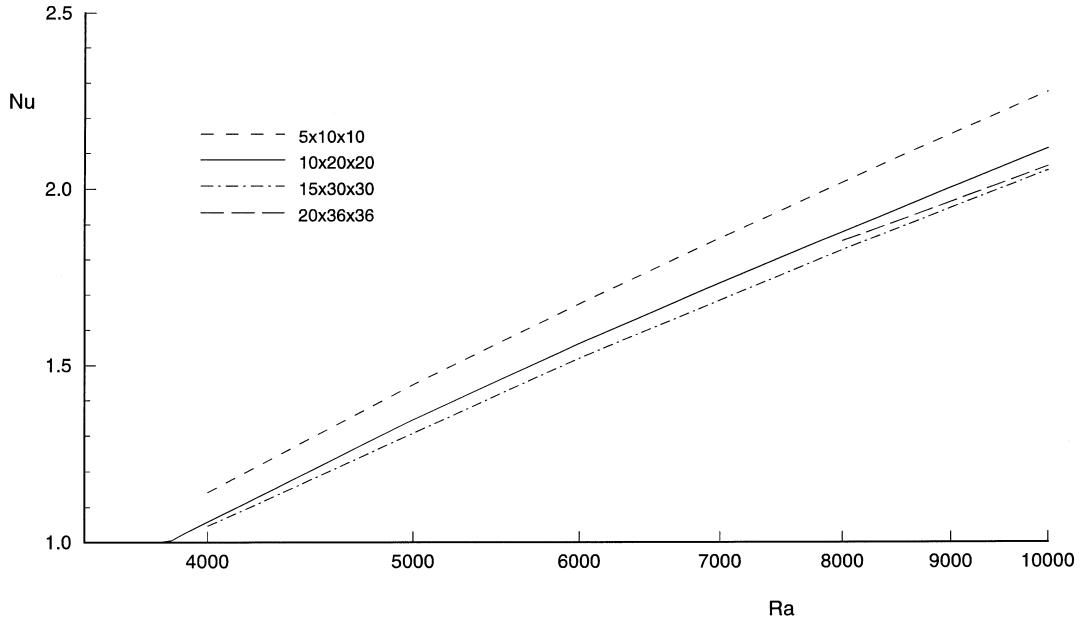

Fig. 11. Average Nusselt number vs Rayleigh number for four different grids: $5\times10\times10$, $10\times20\times20$, $15\times30\times30$ and $20\times36\times36$; $A=1$, $Pr=1$.

In the whole range of parameters, where the steady convection is predicted by the numerical code, no dependence on initial conditions or flow history has been observed; for the determined set of parameters one single stable solution exists. This is in accordance with linear stability theory that predicts only one stable solution in the chosen range of parameters.

The Nusselt number has been used as a criteria looking for the critical Ra value, if $Ra \leqslant Ra_{cr}$ then $Nu=1$. The searching for Ra_{cr} starts with the calculation for slightly supercritical Ra (about $1.2Ra_{cr}$ after Buell and Catton [3]). When the converged solution is obtained the condition $(Nu-1) < 1\cdot10^{-5}$ is checked. If this condition is not satisfied, the Rayleigh number is decreased and the calculation is repeated using the previous solution as the initial guess. The process of gradual decreasing of the Rayleigh number is repeated until the above mentioned condition is satisfied. All the Nusselt numbers stated in this paper (see Nomenclature) are checked in three different cross-sections: on the bottom ($z=0$), at the middle plane ($z=H/2$) and on the top ($z=H$). The difference found between them has been of the order of $O\sim(10^{-6})$ or less.

The numerical data are in good agreement with experimental data and with the results based on linear stability theory found in the literature (Fig. 14). The best coincidence is found with the results of Buell and Catton [3] (discrepancy up to 4%). The results of Charlson and Sani [2] agree well for high aspect ration but near $A=1$ the discrepancy comes up to 16%; this may be explained by the choice of the trial function for asymmetric modes, made in [2]. After Buell and Catton [3] the function used by Charlson and Sani [2] causes the azimuthal component to be zero in the axis what is inadequate for the asymmetric modes (for more details see [3]). The taller the cylinder is the weaker the azimuthal component is, thus the smaller the discrepancy. Our numerical results fit well with the experimental data of Olsen and Rosenberger [6] and Müller and Neumann [8].

Figure 15 shows the numerical data of the Nusselt number, obtained for a $Pr=1$ and a perfectly insulated lateral wall, for different aspect ratios. Not only flow stability is conditioned by the aspect ratio, but also the increase of Nu number value is affected. The resulting values from a correlation created by Schneider and Straub [14] are plotted in the same figure; the correlation, restricted to a vertical cylinder, can be written as:

$$Nu = 1+0.323A^{9/4}\left(\frac{A-0.1}{0.9}\right)^{-1/2} +0.42\left[\left(\frac{Ra}{A^3}\right)^{1/4}-5000^{1/4}\right] \quad (18)$$

For $A=1$ the correlation agrees well, within 5%, with our numerical results up to $Ra=4\cdot10^4$; after this value discrepancy becomes important. For $A=2$, which is a limiting value of the correlation validity, a significant difference exists in the whole range of Ra. To check our results we repeat the calculation for a few Ra values refining the grid by a factor of 8. The supplemental results

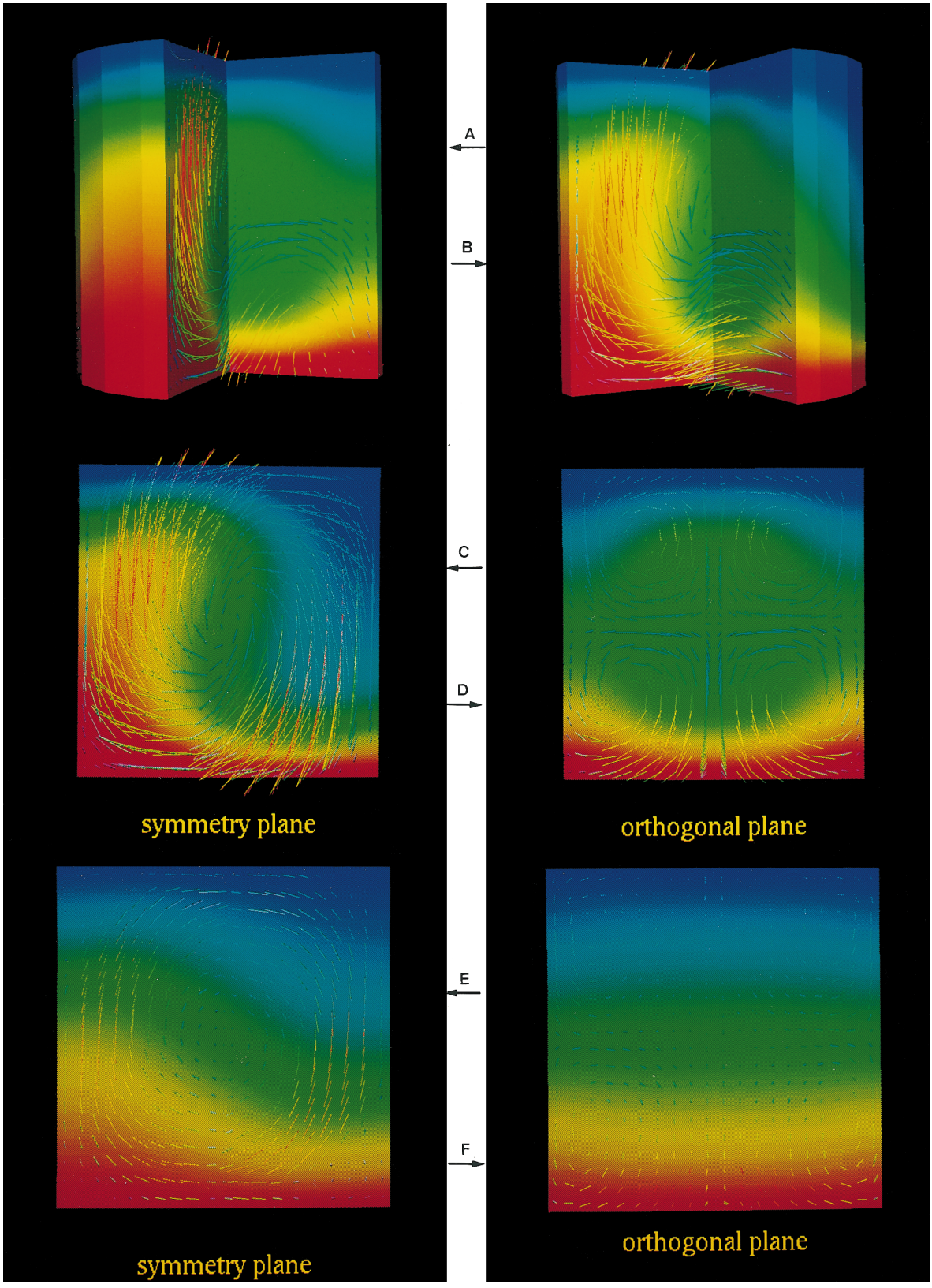

Fig. 12. Isotherms and velocities for $A = 1$, $Ra = 1 \cdot 10^4$; (a) and (b) $Pr = 1$, spatial view with symmetry and orthogonal sections; (c) $Pr = 1$, symmetry plane; (d) $Pr = 1$, orthogonal plane; (e) $Pr = 1 \cdot 10^{-2}$, symmetry plane; (f) $Pr = 1 \cdot 10^{-2}$, orthogonal plane (the surface color in accordance with temperature; the arrow color in accordance with intensity of velocity vector).

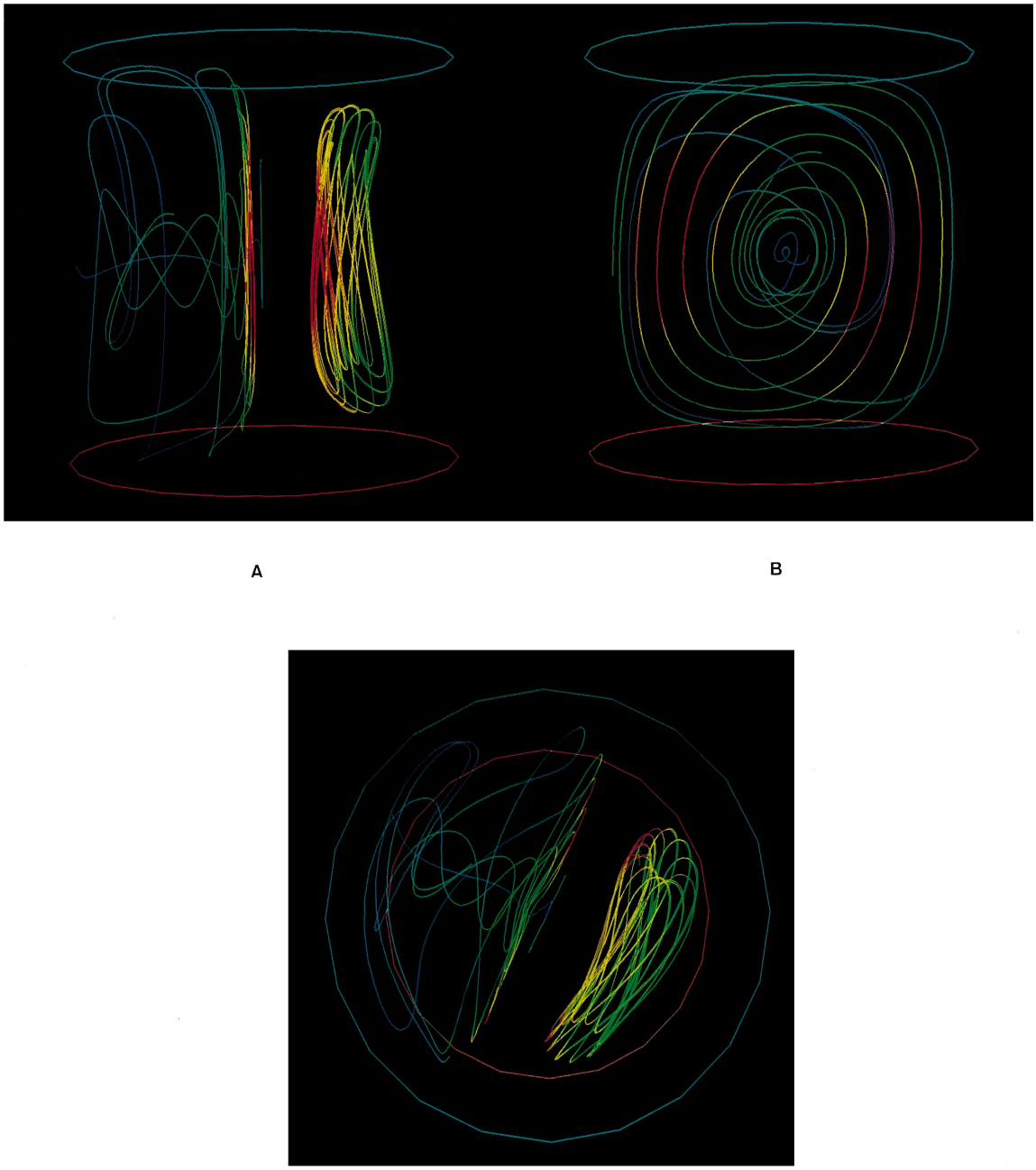

Fig. 13. Typical trajectories for $A = 1$, $Pr = 1$, $Ra = 1 \cdot 10^4$; (a) view from the symmetry plane; (b) view from the orthogonal plane; (c) view from the upper side; (the color in accordance with intensity of velocity vector).

are in accordance with the previous within 3%. The reason for the discrepancy between the present results and the ones obtained by the correlation (18) lies in two facts: one is that the correlation is based on the results obtained on a much coarser grid (grids of $4 \times 8 \times 6$ and $7 \times 10 \times 10$ are stated by Schneider and Straub in [14]) and another is the use of the hybrid numerical scheme in ref. 14, which is essentially first order accurate.

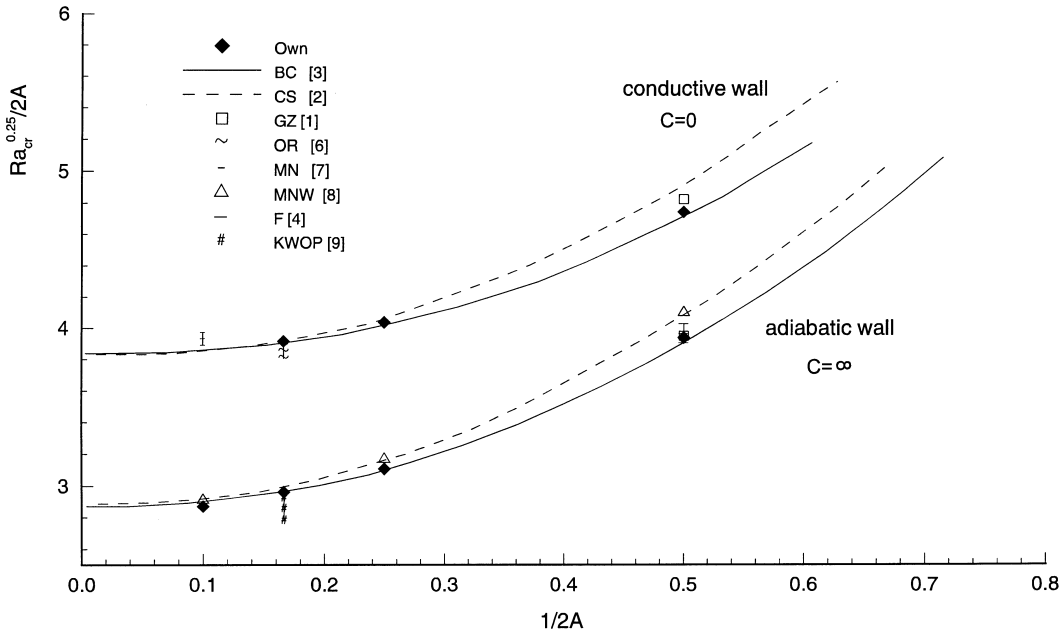

Fig. 14. Critical Rayleigh number vs aspect ratio, stability limit curves for adiabatic and perfectly conducting wall; comparison with other authors: GZ [1], CS [2], BC [3]—linear stability theory, OR [6], MN [7], MNW [8], KWOP [9]—experimental.

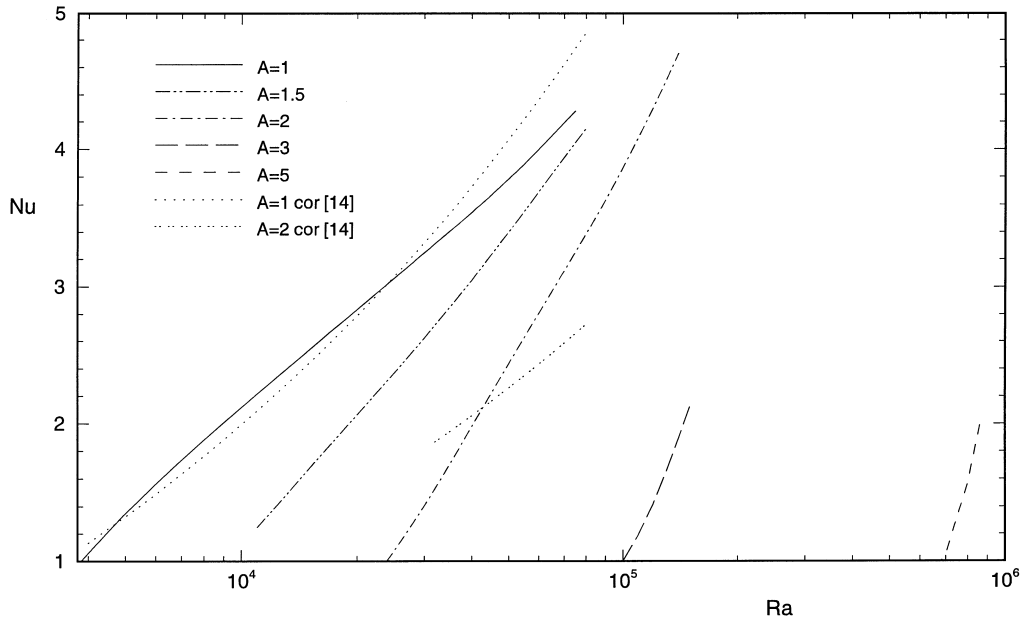

Fig. 15. Average Nusselt number vs aspect ratio; correlation from ref. 14 also depicted.

4.3. Influence of Prandtl number

The Prandtl number influence on heat transfer has been analysed in cylinders of aspect ratio equal to 1. The onset of the first convective instability does not depend on the Prandtl number, but once the motion is established, there is a difference in the flow patterns and Nusselt number. For $Pr \geqslant 0.5$ the influence of Prandtl number on heat transfer is minor; in that range of Pr number, the role of convection is decisive while diffusion has no great importance. To make the distinction between the curves for $Pr = 1$, 10, $1 \cdot 10^3$ and $1 \cdot 10^5$ visible a part of Fig. 16 is magnified; even in this way the difference for $Pr = 1 \cdot 10^3$ and $1 \cdot 10^5$ is indistinguishable. In general, the difference in Nu becomes smaller for high Rayleigh numbers (Fig. 16). The influence of convection on the heat transfer greatly decreases for $Pr < 0.5$, and thermal diffusion becomes the dominant effect. In Figs 12C–F, the isothermal surfaces are plotted for $Pr = 1$ and $1 \cdot 10^{-2}$ respectively. The temperature profile for the low Prandtl number fluid is almost stratified because it is established mainly by diffusion and the isotherms remain less affected by the convection motion.

Appearance of the secondary vortices in the vertical symmetry plane depends on the fluid Prandtl number: for lower Pr fluid vortices come out with smaller Ra. The presence of secondary rolls is indicated in Fig. 16. In the experimental work of Müller et al. [8] this occurs at $Ra \geqslant 5Ra_{cr}$ for water ($Pr = 6.7$), which matches well with our numerical prediction.

The validity of the correlation (18) in its original form [14], including inclined cylinders, has been limited to fluids with $Pr \geqslant 0.7$. Figure 16 suggests that for vertical cylinders of $A = 1$, as a particular case, the application of the correlation may be extended to gases in general (the Prandtl number for gases $Pr \geqslant 0.5$). The difference between Nusselt numbers for $Pr = 1$ and $Pr = 0.5$ is less than 2% for $Ra \leqslant 1 \cdot 10^4$ and less than 1% for the range $1 \cdot 10^4 < Ra < 5 \cdot 10^4$. Obviously, the liquid metals ($Pr \leqslant 0.05$) do not obey the same law. Figure 17 shows plots of Nusselt number vs Prandtl for various Ra. The Nusselt number shows an asymptotic trend with an increase of the Pr.

The other important aspect of Prandtl number influence on flow structure is the oscillatory flow instability, which is considered in the next section.

4.4. Oscillatory flow

When the Rayleigh number is increased to reach a certain value (Ra_{osc}), the phenomenon becomes time-dependent. Over this limit the flow can be laminar (periodic or quasiperiodic) or turbulent. There are several possible scenarios of transition from steady state to turbulence; a good review of this topic is given by Yang [25].

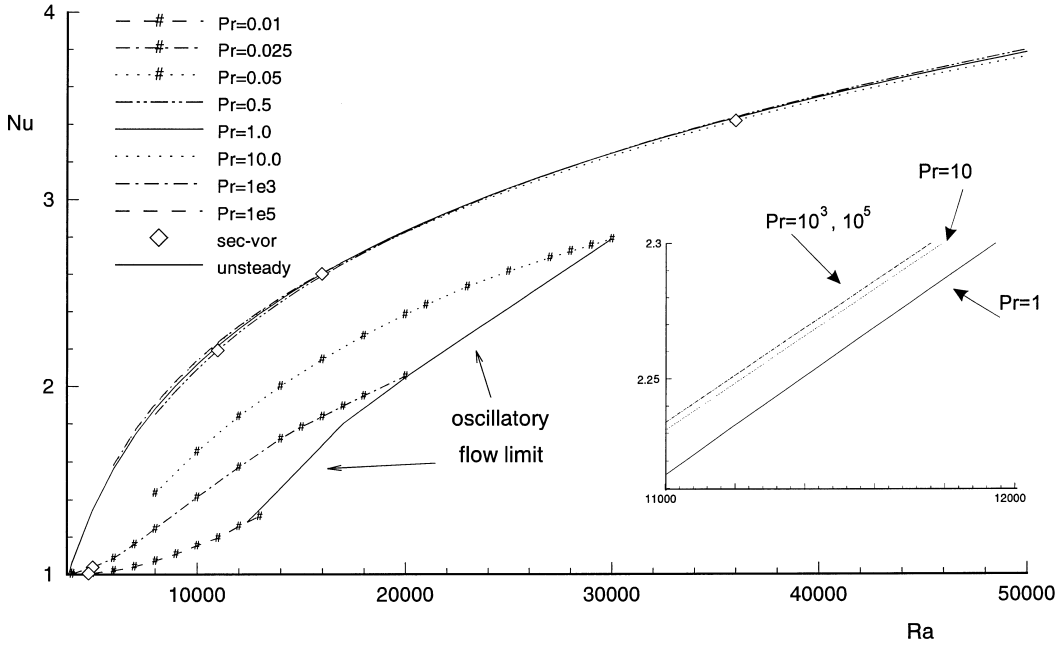

Fig. 16. Average Nusselt number vs Rayleigh number for various Pr; $A = 1$, adiabatic sidewall. For $Pr \leqslant 0.05$ oscillatory flow limit is denoted. Appearance of secondary vortices in the symmetry plane is also indicated (◇).

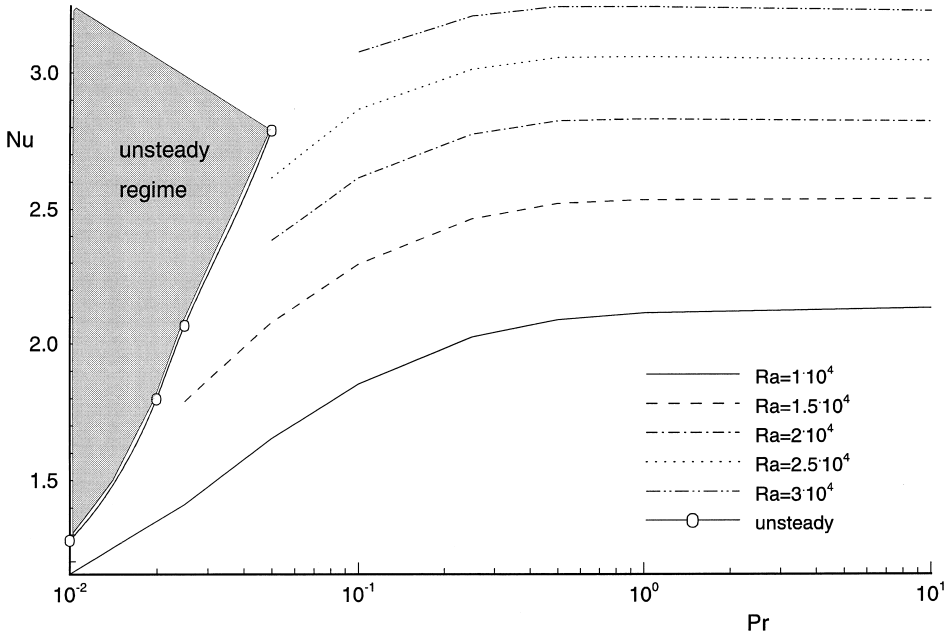

Fig. 17. Average Nusselt number vs Prandtl number for various Ra; oscillatory flow limit; $A = 1$, adiabatic sidewall.

The transition to time-dependent flow in vertical cylinders is affected by the aspect ratio, the Prandtl number and the lateral wall thermal boundary condition. In order to find the oscillatory limit, the Rayleigh number has been increased gradually, in steps of $1 \cdot 10^3$. As the numerical calculation produces unavoidable round-off error it has been considered that this error is enough to provoke oscillatory flow; no other disturbance has been introduced.

In the previous papers by Ivančić et al. [27, 28], the results for $A = 1.5$ and 2, for $Pr = 1 \cdot 10^{-2}$ were presented. The frequencies found for $A = 2$ were in excellent agreement with the experiments of Kamotani et al. [9], the discrepancy was within the measurement error estimated in [9]. For $A = 1.5$ we have no experimental data, but it may be concluded that the frequencies founded are of the same order of magnitude as these presented by Kamatoni et al. for aspect ratios $A = 2$ and 3. For the both aspect ratios the laminar–turbulent transition route is identified as the quasiperiodic one [27, 28].

In the present study the aspect ratio and the lateral wall boundary condition are fixed ($A = 1$), adiabatic boundary condition and the analysis is concentrated on the Prandtl number influence on the time-dependent convection phenomenon. The calculation has been carried out for $1 \cdot 10^{-2} \leqslant Pr \leqslant 1 \cdot 10^{-1}$. For the low Prandtl number fluids, the inertial forces play a dominant role, while the buoyancy forces, induced by the temperature boundary conditions, are less important; with the increase of Pr, inertial forces become less and less influent. Oscillatory phenomenon in low Prandtl number flows comes out due to inertial effects: the lower the Pr number is, the more sensitive the fluid is to oscillatory onset i.e. onset occurs for the lower Rayleigh number. The oscillatory flow limit (Ra_{osc}) increases with the increasing of the Prandtl number; it is depicted in Figs 16 and 17. The oscillatory instability for $Pr = 1 \cdot 10^{-2}$ begins near $Ra_{osc} = 1.3 \cdot 10^4$ and for $Pr = 5 \cdot 10^{-2}$ near $Ra_{osc} = 3 \cdot 10^4$. The fundamental frequency of the periodic flow grows with the rise of the Prandtl number. Indications of oscillatory flow have not been found for $Pr \geqslant 0.1$, in the studied range of the Rayleigh number.

The dynamic behavior of time-dependent flow has been examined using the power spectra. The same frequencies have been found in all nodes which means that the movement in the whole cylinder is synchronized. The mean Nusselt number on the hot and cold bases are in opposite phase. The biggest amplitudes are detected near the sidewall, in the top and bottom of the cavity (in the cavity corners). As can be seen in Fig. 18, the frequency of oscillations shows a weak dependence on the Rayleigh number in the range $1.7 \cdot 10^4 \leqslant Ra \leqslant 1.8 \cdot 10^4$; it increases the growth of the Ra.

Certain influence of time step on frequency has been observed. The frequencies for three runs with different times steps are presented in Table 2 ($Pr = 2 \cdot 10^{-2}$, $Ra = 1.7 \cdot 10^4$). The frequency increases when the time step is shortened. The other outstanding effect of decrementing the time step is the presence of a new important

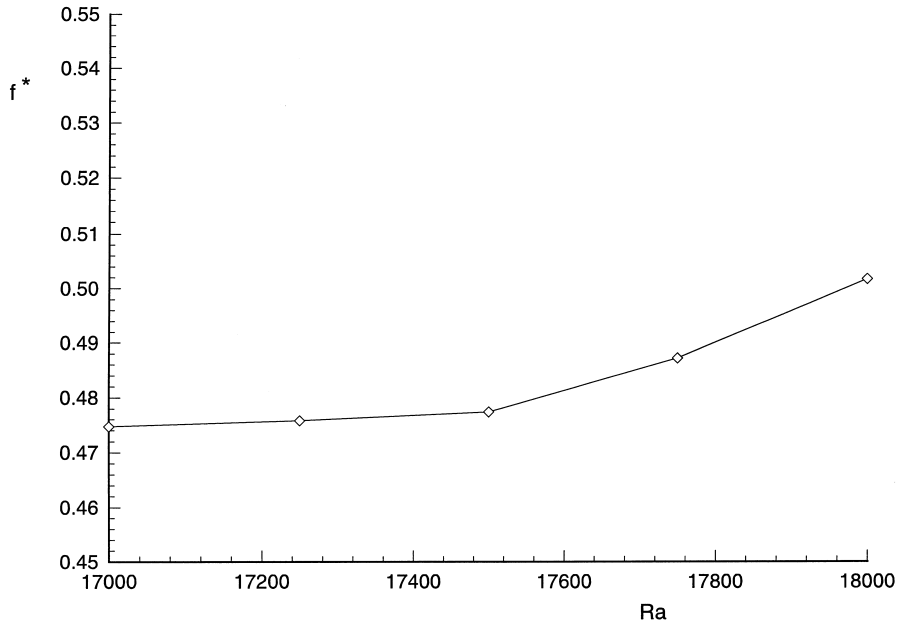

Fig. 18. Dimensionless fundamental frequency vs Rayleigh number; $Pr = 2 \cdot 10^{-2}$.

Table 2
Dimensionless frequency vs dimensionless time step for $Ra = 1.7 \cdot 10^4$ and $Ra = 1.8 \cdot 10^4$, $Pr = 2 \cdot 10^{-2}$; the frequencies are made dimensionless multiplying by H^2/α

	t	0.1	0.05	0.01
	t^*	$1.83 \cdot 10^{-3}$	$9.15 \cdot 10^{-4}$	$1.83 \cdot 10^{-4}$
$Ra = 1.7 \cdot 10^4$	f^*	0.453	0.474	0.475
$Ra = 1.8 \cdot 10^4$	f^*	—	0.490	0.502

harmonic of the fundamental frequency which has been omitted in the simulation with the longer time step.

4.5. Influence of the lateral wall thermal boundary condition

The results obtained by the numerical code for conjugated heat transfer problem were first contrasted with experimental data [8] and linear stability theory predictions [3] comparing the critical Rayleigh number for different wall admittances. Afterwards the analysis for aspect ratios $A = 1$ and $A = 2$ has been accomplished.

The influence of the solid wall thickness and its thermal conductivity is treated by means of the wall admittance C, a dimensionless parameter defined above. The idealised extremes ($C = 0$ for a perfectly conducting wall and $C = \infty$ for a perfectly insulating wall) can be calculated imposing suitable boundary condition on fluid domain without taking into account the solid wall. To analyse the situations in between these two extremes the thermal conduction through the solid wall must be involved in calculation.

Figure 19 shows the critical Rayleigh number vs aspect ratio for different C. The simulation of the flow inside the cylinder of wall admittance $C = 1$ and $C = 10$ gives somewhat lower values of critical Rayleigh number than those presented in [3] (Fig. 19). For $A = 1$ the convective threshold is found to occur for a Ra 10–15% smaller. For $A = 5$ the numerical results are in good agreement with experimental data measured by Müller and Neumann [7], while considerable disagreement with the linear stability theory predictions by Buell and Catton exists. The experimental results of Cane et al. [26] for a tall cavity with square and hexagonal base and $C = 10$ are also depicted; the results correspond to the geometry with the same hydraulic diameter as the numerical results presented for the cylinder. The fact that the critical Ra values for these three geometries are very similar, all the results within 6% of difference, shows that the geometry of the cavity base is a factor of minor influence on convective onset in high aspect ratio cavities.

The structure of the first convective motion that appears is independent on wall admittance, in the studied range of aspect ratio, and corresponds to the motion described above (Fig. 13). The conduction through the lateral wall gives additional stability to the fluid layer. The critical Rayleigh number is 2–3 times higher for $C = 0$ than that found for $C = \infty$.

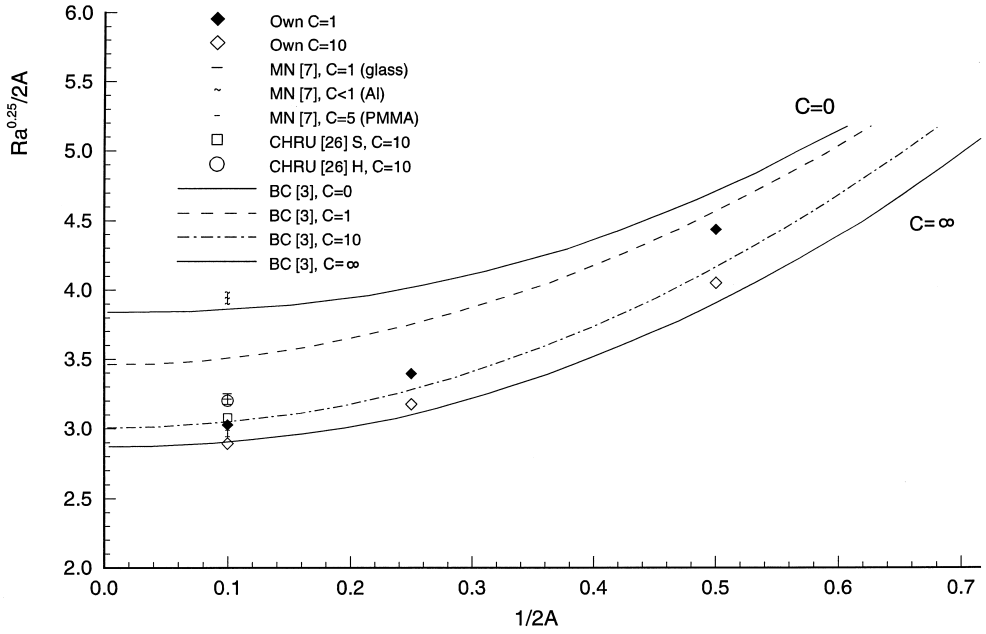

Fig. 19. Critical Rayleigh number vs aspect ratio, stability limit curves for $C = 1$ and $C = 10$; comparison with data from: BC [3]—linear stability theory, MN [7]—experimental, CHRU [26]—experimental for the square and hexagonal cavities for $C = 10$.

In Figs 20 and 21 the Nusselt number vs the Rayleigh number for two aspect ratios ($A = 1$ and $A = 2$ respectively) are given. When the Rayleigh number is increased, secondary vortices in the symmetry plane appear first for perfectly conducting sidewall, at very low Rayleigh number ($Ra \approx 1.1Ra_{cr}$). For less conductive sidewall, vortices come out for higher Ra and develop slower with an increase of the Ra than these for $C = 0$. The lower

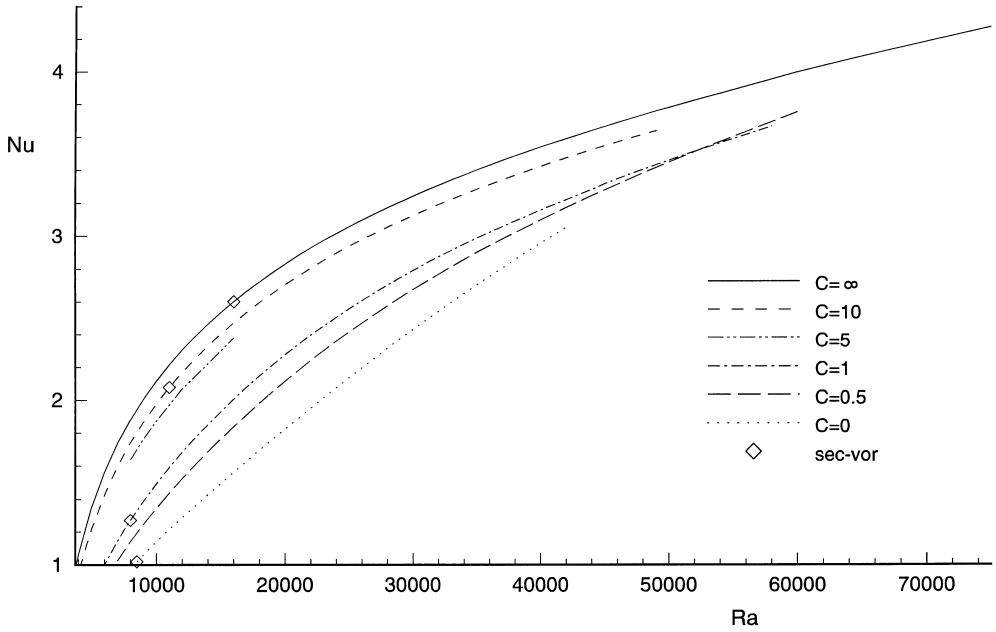

Fig. 20. Average Nusselt number vs Rayleigh number for various C; $Pr = 1$, $A = 1$; appearance of secondary vortices in the symmetry plane also indicated (◇).

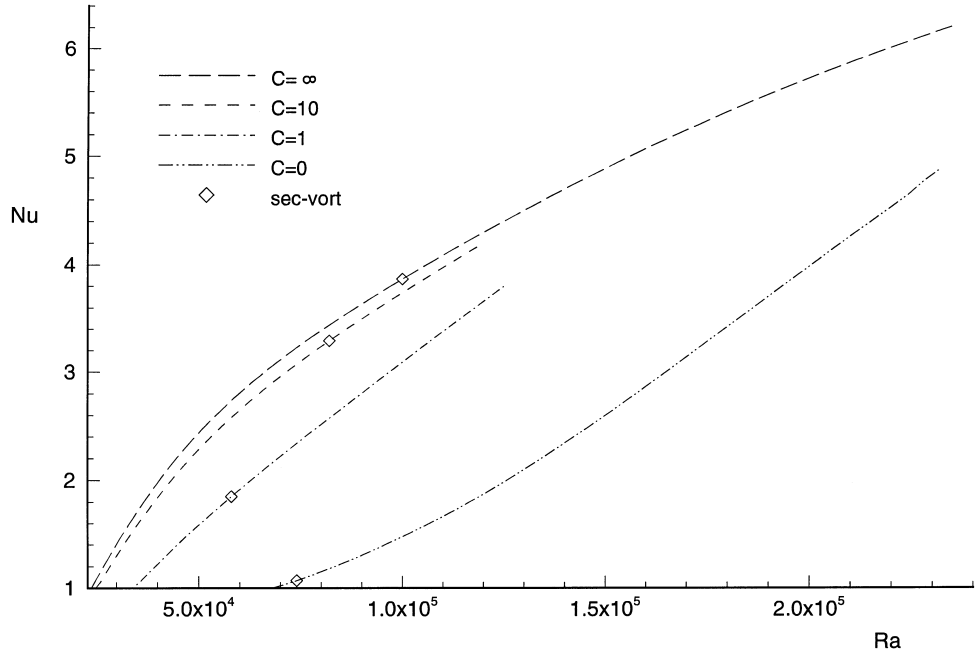

Fig. 21. Average Nusselt number vs Rayleigh number for various C; $Pr = 1$, $A = 2$; appearance of secondary vortices in the symmetry plane also indicated ($\diamond$).

wall admittance increases fluid stability with respect to the first convective motion. Interestingly, once the motion is established, the conducting wall thermal effect increments the growth of the Nusselt number with the rise of Ra (Fig. 20). The Nusselt number for more conducting lateral wall then exceeds the one resulting from adiabatic boundary condition. This can be explained by the conducting wall thermal effects that introduce additional buoyancy near the cylinder bases. As a consequence, more developed secondary vortices are present in the symmetry plane.

For the unit aspect ratio, the crosspoint of curves $Nu(Ra)$ regarding $C = 0$ and $C = \infty$ takes place at $Ra \approx 6.9 \cdot 10^4$. When $Ra < 6.9 \cdot 10^4$ heat transfer is more intensive for the adiabatic wall configuration, on the other hand for $Ra > 6.9 \cdot 10^4$ conducting wall configuration provokes higher Nu. The maximum velocity for $C = 0$ configuration becomes greater than the maximum value for $C = \infty$ near $Ra \approx 5.5 \cdot 10^4$. The flow in a cavity with $A = 2$ exhibits a similar trend but the crosspoint of $Nu(Ra)$ curves has not been achieved in the range of Ra studied here (Fig. 21).

5. Conclusions

The purpose of the present work has been to study the effects of the Rayleigh number, Prandtl number, aspect ratio and lateral wall thermal boundary condition on the laminar natural convection in a vertical cylinder heated from below.

The treatment of the Navier–Stokes equations written in cylindrical coordinates has been given for cases when the physical boundary does not agree with the coordinate origin ($r = 0$). The numerical code has been validated for two test situations giving satisfactory results. The chosen approach shows good numerical stability and offers results that, in general, agree closely with the experimental data and the linear stability theory predictions. It has been shown that the selected grid is sufficient for qualitative analysis of the phenomenon even if the grid independent solution has not been achieved.

For steady convection no dependence of flow structure and Nu on flow history has been observed, which is in accordance with linear stability theory that predicts only one stable solution in the chosen range of parameters.

The study of Prandtl number effect on heat transfer shows that for most technical applications the influence of Prandtl number for $Pr \geqslant 0.5$ could be neglected. For $Pr < 0.1$ the Nusselt number exhibits different behaviour depending strongly on Pr.

For low Prandtl number fluids, the time-dependent flow has been detected; this kind of oscillations is a consequence of the inertial effects. As Pr increases, the oscillation onset arises for higher Ra and with higher fundamental frequency. In general, oscillations are more pronounced in the cavity corners.

The critical Rayleigh number depends on the lateral

thermal boundary condition, i.e. physical properties of sidewall material and its geometry, but the structure of the first convective motion does not.

The influence of lateral wall thermal boundary conditions on Nusselt number has also been analysed. It may be a very significant factor in heat transfer because the lateral wall conduction can increase or decrease the heat flux through the fluid layer and the maximum velocity in it; it depends on Ra. After Ra_{cr}, $C = \infty$ case gives higher Nu, but afterwards the velocities increase more rapidly for $C = 0$ and, consequently, Nu for that configuration becomes higher.

Future work will be aimed to extend the analysis the wider range of parameter space (A and C) and thereafter to correlate the obtained results.

Acknowledgements

This study has been supported by the Direcció General de Recerca, program: Ajuts a les universitats públiques catalanes per la contractació de tècnics qualificats de suport a la recerca and the Dirección General de Investigación Científica y Técnica (ref. no. PB90-0606).

References

[1] Gershuni GZ, Zhukovitskii EM. Convective stability of incompressible fluids. Jerusalem: Keterpress Enterprises, 1976.

[2] Charlson GS, Sani RL. On thermoconvective instability in a bounded cylindrical fluid layer. Int J Heat Mass Transfer 1971;14:2157–60.

[3] Buell JC, Catton I. The effect of wall conduction on the stability of a fluid in a right circular cylinder heated from below. J of Heat Transfer 1983;105:255–60.

[4] Figliola RS. Convection transitions within a vertical cylinder heated from below. Phys Fluids 1986;29:2028–31.

[5] Azouni MA, Grenet JP. Observation visuelle de la convection naturalle dans une cavite cylindrique de hauteur variable. Proc 6th Europ Symp on Materials Sciences under Microgravity Conditions. ESA SP-256, Bordeaux, 1986, pp. 547–9.

[6] Olson JM, Rosenberger F. Convective instabilities in a closed vertical cylinder heated from below. Part 1. Monocomponent gases. J Fluid Mech 1979;92:609–29.

[7] Müller G, Neumann G. Investigation of convective flows in model systems of directional solidification configurations. Proc 4th Europ Symp on Materials Sciences under Microgravity Conditions. ESA SP-191, Madrid, 1983, pp. 285–93.

[8] Müller G, Neumann G, Weber W. Natural convection in vertical Bridgman configurations. J Crystal Growth 1984;70:78–93.

[9] Kamotani Y, Weng FB, Ostrach S, Platt J. Oscillatory natural convection of a liquid metal in circular cylinders. J of Heat Transfer 1994;116:627–32.

[10] Crespo Del Arco E, Bontoux P, Sani RL, Hardin G, Extremet GP, Chikhaoui A. Finite difference solution for three-dimensional steady and oscillatory convection in vertical cylinders—effects of aspect ratio. Natural Convection in Enclosure ASME HTD 1988;99:647–76.

[11] Crespo Del Arco E, Bontoux P. Numerical solution and analysis of asymmetric convection in a vertical cylinder: an effect of Prandtl number. Phys Fluids A 1989;1:1348–59.

[12] Crespo Del Arco E, Bontoux P, Smutek P, Roux C, Hardin G, Sani RL, Rosemberger F. Three-dimensional simulations of convective regimes in cylindrical ampoules. Comparison with theoretical analysis and experiments. Proc 6th Europ Symp on Materials Sciences under Microgravity Conditions. ESA SP-256, Bordeaux, 1986, pp. 529–37.

[13] Neumann G. Three-dimensional numerical simulation of buoyancy-driven convection in vertical cylinders heated from below. J Fluid Mech 1990;214:559–78.

[14] Schneider S, Straub J. Laminar natural convection in a cylindrical enclosure with different end temperatures. Int J Heat Mass Transfer 1992;35:545–57.

[15] de Vahl Davis G. A note on a mesh for use with polar coordinates. Numerical Heat Transfer 1979;2:261–6.

[16] Leong SS, de Vahl Davis G. Natural convection in a horizontal cylinder. Proc Numerical Meth Thermal Problems I. Pineridge, Swansea, 1979, pp. 287–96.

[17] Bontoux P, Smutek C, Roux B, Lacroix JM. Three-dimensional buoyancy driven flows in cylindrical cavities with differentially heated endwalls 1. Horizontal cylinders. J Fluid Mech 1986;169:211–27.

[18] Van Doormaal JP, Raithby GD. Enhancements of the simple method for predicting incompressible fluid flow. Numerical Heat Transfer 1984;7:147–63.

[19] Patankar SV. Numerical heat transfer and fluid flow. Washington D.C.: Hemisphere, 1980.

[20] Schneider GE, Zedan M. A modified strongly implicit procedure for the numerical solution of field problems. Numerical Heat Transfer 1981;4:1 – 19.

[21] Leonard BP. A stable and accurate convective modelling procedure based on quadratic upstream interpolation. Comp Meth in Appl Mech and Eng 1979;19:59–95.

[22] Gaskell PH, Lau AKC. Curvature-compensated convective transport: SMART, a new boundedness-preserving transport algorithm. Int J Numerical Methods Fluids 1988;8:617–41.

[23] Koschmieder EL. Bénard convection. Adv Chem Phys 1974;26:177–211.

[24] Kessler R. Nonlinear transition in three-dimensional convection. J Fluid Mech 1987;174:357–79.

[25] Yang KT. Transitions and bifurcations in laminar buoyant flows in confined enclosure. J of Heat Transfer 1988;110:1191–204.

[26] Cane RLD, Hollands KGT, Raithby GD, Unny TE. Free convection heat transfer across inclinated honeycomb panels. J of Heat Transfer 1977;99:86–91.

[27] Ivančić A, Oliva A, Pérez-Segarra CD, Schweiger H. Numerical simulation of oscillatory regimes in vertical cylinders heated from below. Notes on numerical fluid mechanics 1995;53:102–8.

[28] Ivančić A, Oliva A, Pérez-Segarra CD, Schweiger H. Transition regimes for buoyancy driven flows in vertical cylinders. Numerical experiments, to appear.

[29] Khosla PK, Rubin SG. A diagonally dominant second-order accurate implicit scheme. Comput Fluids 1974;2:207–9.
[30] Smith RM, Hutton AG. The numerical treatment of advection: a performance comparison of current methods. Numerical Heat Transfer 1982;5:439–61.
[31] Van Leer B. Toward the ultimate conservative difference scheme V. A second-order sequel to Godunov's method. J Comp Physics 1977;23:101–36.
[32] Zhu J, Rodi W. A low dispersion and bonded convection scheme. Comp Metho Appl Mech Eng 1991;92:87–96.